

Hierarchy of chaotic dynamics in random modular networks

Łukasz Kuśmierz,¹ Ulises Pereira-Obilinovic,¹ Zhixin Lu,¹ Dana Mastrovito,¹ and Stefan Mihalas¹

¹Allen Institute, Seattle, WA

We introduce a model of randomly connected neural populations and study its dynamics by means of the dynamical mean-field theory and simulations. Our analysis uncovers a rich phase diagram, featuring high- and low-dimensional chaotic phases, separated by a crossover region characterized by low values of the maximal Lyapunov exponent and participation ratio dimension, but with high values of the Lyapunov dimension that change significantly across the region. Counterintuitively, chaos can be attenuated by either adding noise to strongly modular connectivity or by introducing modularity into random connectivity. Extending the model to include a multilevel, hierarchical connectivity reveals that a loose balance between activities across levels drives the system towards the edge of chaos.

Introduction.—Natural and artificial systems at the edge of chaos exhibit unique computational properties [1–4]. For instance, placing artificial neural networks at the edge of chaos has been shown to optimize learning and information processing in various scenarios [5–10]. Accordingly, it has been suggested that neural circuits in the brain operate at, or remain near to, a critical point such as the edge of chaos [11–19], which may explain some aspects of the structure of the variability observed in neural recordings. However, keeping complex systems at a critical point is challenging, as it is usually sensitive to external or internal changes, such as noise and external inputs [10, 20–22], or low-rank structural connectivity perturbations [23–30]. How can complex systems be robustly maintained at the edge of chaos? In the context of neuroscience, synaptic plasticity has been suggested as the underlying feedback mechanism driving neural circuits towards a critical point [31–34]. It is unclear, however, whether synaptic plasticity mechanisms can drive networks specifically to the edge of chaos [35] and how the underlying connectivity organization affects the type and robustness of the emergent critical behavior.

Hierarchical organization is common in biological and artificial complex systems, including brains, ecosystems, and artificial neural networks. Mammalian brains are modular and hierarchical [36–41], and are composed of many distinct cell types that themselves are hierarchically organized [42, 43]. The hierarchical organization of the visual system [44] has inspired the design of computationally powerful artificial neural network architectures [45], which are similarly hierarchically structured [46]. Ecological systems, including food webs, also exhibit hierarchical organization [47]. How does hierarchical organization affect the collective behavior of such complex systems? Simulation studies suggest that hierarchical modular connectivity broadens the parameter space supporting critical-like behavior [48–50], but the exact mechanism, its universality, and its relation to the edge of chaos remain unclear.

Thus, we set out to understand how modular and hierarchical connectivity organization affects dynamics at different levels of the hierarchy. As we demonstrate below, the presence of modules gives rise to qualitatively distinct chaotic phases. High-dimensional chaotic activity (microscopic chaos) common in homogeneous networks [51, 52] is separated from the

low-dimensional chaotic activity of strongly coherent modules (macroscopic chaos) by an interesting crossover region (multiscale chaos), wherein both forms of chaotic activity coexist and the dimension of activity can be interpreted as either high or low, depending on the measure used. Furthermore, random hierarchical interaction structures significantly enhance the robustness of the edge of chaos without the need for precise fine tuning. The underlying mechanism is remarkably simple: Different levels of the hierarchy effectively compete for activity and the hierarchical organization in the network’s interactions coarse-grains chaotic fluctuations from lower levels to higher ones, preventing the amplification of chaos at higher levels in the hierarchy.

Model.—We study a class of random network models commonly used in neuroscience [51], artificial intelligence [7, 53], and ecology [54–56], incorporating modular and hierarchical organization into their interactions. We structure these interactions in levels, where higher levels are constructed by coarse-graining lower levels. Despite the generality of the model, for concreteness we refer to nodes of the network as neurons and to interaction strengths between them as synaptic weights. We start by introducing and analyzing a two-level modular system, in which the interaction matrix is generated in blocks corresponding to distinct populations, i.e. clusters of neurons with similar connectivity patterns. In effect, populations are introduced through a random and relatively low-rank connectivity perturbation [57, 58] and, in the context of neuroscience, can be interpreted as emerging from shared spatial locations, morphologically or genetically defined cell types, or functions as in neuronal ensembles or engrams. Later we generalize our model and analysis by incorporating multiple levels.

Since we focus our attention on the effects of connectivity patterns, we choose a simple rate model with dynamics shared across all populations:

$$\mathbf{x}(t+1) = \phi(\mathbf{J}\mathbf{x}(t)) \quad (1)$$

where $\mathbf{x}(t)$ is a vector of neural activity at time t , \mathbf{J} is the connectivity matrix, and the activation function $\phi : \mathbb{R} \rightarrow \mathbb{R}$ is applied element-wise. We take \mathbf{J} to be a block matrix of the

form

$$J = \begin{bmatrix} J^{11} & J^{12} & \dots & J^{1P} \\ J^{21} & J^{22} & \dots & J^{2P} \\ \vdots & \vdots & \ddots & \vdots \\ J^{P1} & J^{P2} & \dots & J^{PP} \end{bmatrix} \quad (2)$$

where each block $J^{\alpha\beta}$ is a submatrix that contains all synaptic weights from neurons in population β to all neurons in population α . For simplicity of notation, here we limit our attention to P populations of the same size n [59].

To obtain a minimal and solvable model with characteristics of population-specific connectivity patterns, we define a hierarchical weight-generating process as follows. We endow each pair of populations (α, β) with a pair of parameters $(\mu^{\alpha\beta}, \sigma^{\alpha\beta})$ which are used to generate random weights between neurons in these populations as $J_{ij}^{\alpha\beta} \sim \mathcal{N}(\mu^{\alpha\beta}/n, \sigma^{\alpha\beta}/\sqrt{n})$. These pairs of parameters are themselves generated randomly i.i.d. from a specific distribution. In this work we focus our attention on the case of $\sigma^{\alpha\beta} = \sigma/\sqrt{P}$ fixed and shared across all pairs of populations and $\mu^{\alpha\beta}$ generated randomly as $\mu^{\alpha\beta} \sim \mathcal{N}(0, \sigma_\mu/\sqrt{P})$. The overall connectivity matrix can be concisely expressed as

$$J = \sigma_\mu \Xi^{(P)} \otimes O^{(n)} + \sigma \Xi^{(N)} \quad (3)$$

where \otimes stands for the Kronecker product, $N = nP$ is the total number of neurons, $O^{(n)} = vv^T$ is a fixed $n \times n$ orthogonal projection matrix with $v^T = \frac{1}{\sqrt{n}} [1 \ 1 \ \dots \ 1]$, and $\Xi^{(m)}$ is a random $m \times m$ matrix with each entry generated i.i.d. from $\mathcal{N}(0, 1/\sqrt{m})$. Note that matrices $\Xi^{(P)}$ and $\Xi^{(N)}$ are mutually independent and correspond to different levels in the hierarchy of randomness: $\Xi^{(P)}$ to mean efficacies between pairs of populations and $\Xi^{(N)}$ to random fluctuations at the level of pairs of individual neurons. The resulting connectivity matrix has a block structure with a double-disk distribution of eigenvalues [58], see Fig. 1.

Mean-field analysis.—In order to enable a straightforward mathematical analysis of the typical behavior of a network with multiple populations of neurons we consider a rather natural limit of a large number of large populations $1 \ll P \ll N$. The activity of neuron i in population α evolves according to (1), which we rewrite as

$$x_i^\alpha(t+1) = \phi(h_i^\alpha(t)) \quad (4a)$$

$$h_i^\alpha(t) = \sum_{\beta=1}^P \sum_{j=1}^n J_{ij}^{\alpha\beta} x_j^\beta(t) \quad (4b)$$

where the input currents (preactivations) can be expressed as

$$h_i^\alpha(t) = \sum_{\beta=1}^P \mu^{\alpha\beta} m^\beta(t) + \sum_{\beta=1}^P \sum_{j=1}^n \sigma \Xi_{ij}^{\alpha\beta} x_j^\beta(t) \quad (5)$$

with i.i.d. $\Xi_{ij}^{\alpha\beta} \sim \mathcal{N}(0, 1/\sqrt{N})$ and where we define the mean activity of population α as

$$m^\alpha(t) = \frac{1}{n} \sum_{i=1}^n x_i^\alpha(t) \quad (6)$$

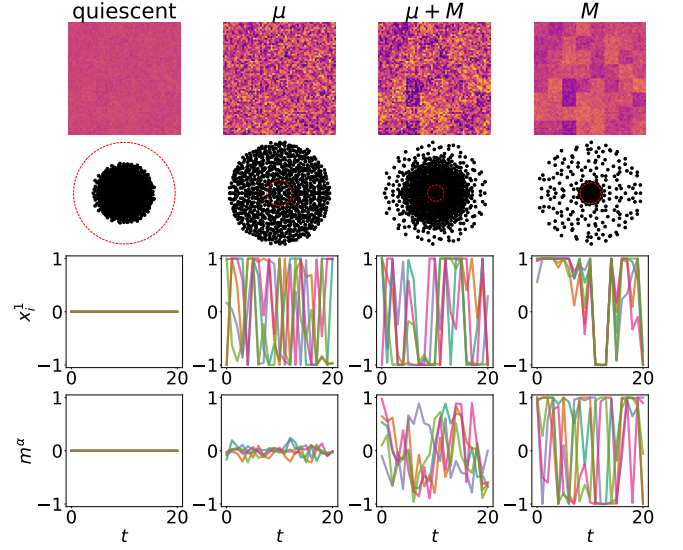


FIG. 1. Visualizations of the weight matrix (*top row*), its eigenvalues (*second row*), and steady-state activities of five sample neurons from a shared population (*third row*) and five sample populations (*bottom row*) in four phases predicted by the mean-field theory: quiescent ($\sigma = \sigma_\mu = 0.5$), μ (microscopic chaos, $\sigma = 4, \sigma_\mu = 0.5$), $\mu + M$ (multiscale chaos, $\sigma = 4, \sigma_\mu = 6$), and M (macroscopic chaos, $\sigma = 1, \sigma_\mu = 5$). Red dashed lines in the eigenvalue spectra represent the unit circle in the complex plane.

When considered as a function of quenched synaptic weight disorder, the input current of each neuron is a Gaussian random variable. To keep track of the correlation structure between different neurons we rewrite it as a sum of population-specific and neuron-specific terms

$$h_i^\alpha(t) = \sigma_\mu \sqrt{q_m(t)} \tilde{z}^\alpha + \sigma \sqrt{q(t)} z_i^\alpha \quad (7)$$

where $\tilde{z}^\alpha, z_i^\alpha$ are i.i.d. standard Gaussian random variables and

$$q_m(t) = \frac{1}{P} \sum_{\alpha=1}^P (m^\alpha(t))^2 \quad (8a)$$

$$q(t) = \frac{1}{N} \sum_{\alpha=1}^P \sum_{i=1}^n (x_i^\alpha(t))^2 \quad (8b)$$

are the order parameters that specify, respectively, the total activity variance, and the variance of mean population activities (macroscopic activity). In order to analyze the evolution of these order parameters we combine the single-neuron evolution equations (4) with (7) and (8), average over quenched disorder, and obtain a coupled pair of mean-field equations (see Appendix A for the derivation)

$$q_m(t+1) = \int D\tilde{z} \left[\int Dz \phi(\sigma_\mu \sqrt{q_m(t)} \tilde{z} + \sigma \sqrt{q(t)} z) \right]^2 \quad (9a)$$

$$q(t+1) = \int Dz \left[\phi(\sqrt{\sigma_\mu^2 q_m(t) + \sigma^2 q(t)} z) \right]^2 \quad (9b)$$

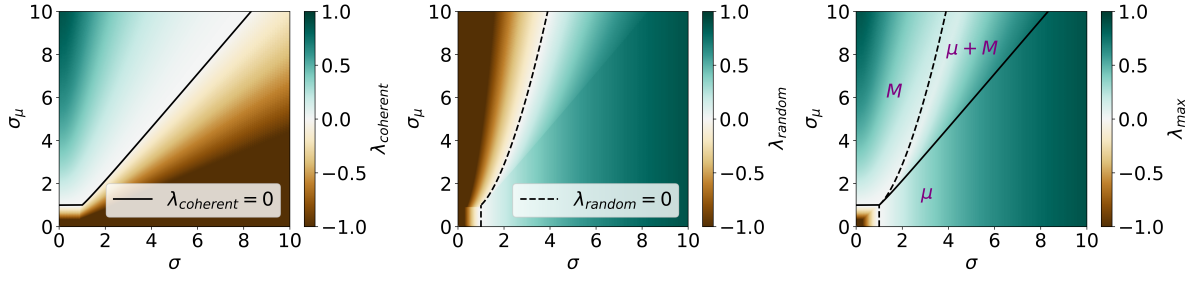


FIG. 2. The mean-field phase diagram. Lines represent transition lines: σ_μ^* (solid) and σ_μ^{EoHC} (dashed). Phases are denoted by symbols M (macroscopic chaos) and μ (microscopic chaos). Heat maps represent the values of $\lambda_{coherent}$ (left), λ_{random} (center), and λ_{max} (right).

where $\int Dz f(z) \equiv \int_{-\infty}^{\infty} dz f(z) \exp(-z^2/2) / \sqrt{2\pi}$. Fixed points (q, q_m) of the mean-field equations (9) specify dynamical regimes (phases) of the network.

Before we proceed with the analysis of the mean-field equations, we note that the mean population activities behave like an effective recurrent neural network, with units corresponding to populations. Indeed, let us combine (4), (5), and (6), take the limit $n \rightarrow \infty$, and apply the law of large numbers, leading to

$$m^\alpha(t+1) = \phi_{\sigma\sqrt{q}} \left(g(\sigma\sqrt{q}) \sum_{\beta=1}^P \mu^{\alpha\beta} m^\beta(t) \right) \quad (10)$$

with $\phi_a(g(a)x) \equiv \int Dz \phi(x + az)$ and $g(a) \equiv \int Dz \phi'(az)$ chosen such that $\phi'_a(0) = \frac{d\phi_a(x)}{dx}|_{x=0} = 1$. These considerations lead to a natural decomposition of network dynamics into two levels: macroscopic dynamics of means (activities of populations) and microscopic dynamics of neurons within populations around the means. A non-zero value of q_m signals that the macroscopic dynamics is non-quiet. We will refer to such dynamics as coherent, since in this case neural activities within populations are correlated. Similarly, a non-zero value of q signals that the overall activity of the network is non-quiet. Finally, $q - q_m$ measures the average level of variability of neural activity within populations (microscopic dynamics).

In the following we assume that ϕ is continuous, odd, and non-decreasing with $\phi(\infty) = 1$ and $\phi'(0) = 1$. Thus, our results apply to the widely used tanh activation function, although in our computer simulations and some of the mathematical analysis we instead specialize to

$$\phi_\infty(x) = \text{erf}\left(\frac{\sqrt{\pi}}{2}x\right) \quad (11)$$

This implies $\phi(0) = 0$, hence $q = q_m = 0$ is a fixed point of the mean-field equations (9). The linearization around this fixed point

$$q_m(t+1) = \sigma_\mu^2 q_m(t) \quad (12a)$$

$$q(t+1) = \sigma_\mu^2 q_m(t) + \sigma^2 q(t) \quad (12b)$$

demonstrates that the quiescent state with $\mathbf{x} = 0$ is stable for $\sigma < 1$ and $\sigma_\mu < 1$. Outside of this regime the fixed point

with $q = q_m = 0$ is unstable and a new stable fixed point with $q > 0$ signals an active state, which can be subdivided into three qualitatively different phases and two associated phase transitions. The first transition is indicated by the bifurcation in the mean-field evolution equation of q_m (9a) at σ_μ^* (for fixed σ). Below the transition ($\sigma_\mu < \sigma_\mu^*$) the fixed point is such that $q_m = 0$, translating into $m^\alpha(t) = 0$ for all populations. In this phase activities within populations are not coherent. Above the transition ($\sigma_\mu > \sigma_\mu^*$) the fixed point with $q_m = 0$ is unstable and a stable fixed point with $q_m > 0$ characterizes the steady state, translating into non-zero mean population activities (coherent chaos [26]). In order to derive an expression for σ_μ^* , we linearize (9) around $q > 0$ and $q_m = 0$ and find

$$\sigma_\mu^* = \frac{1}{g(\sigma\sqrt{q})} = \frac{1}{\int Dz \phi'(\sigma\sqrt{q}z)} \quad (13)$$

Although, as we show below, in this model the active state is necessarily chaotic, we can further distinguish two phases that differ in the nature and dimensionality of the chaotic activity manifold. When the value of σ_μ is relatively low, the corresponding chaotic attractor spans a high dimensional subspace and any random perturbation is rapidly expanded. In contrast, for $\sigma_\mu \gg \sigma$ the chaotic attractor is confined to a relatively low dimensional manifold and perturbations in random directions are contracted with high probability. The directions of expansion are aligned with the macroscopic activity.

Our derivation is based on the analysis of the evolution of an infinitesimal perturbation tracking the activity difference between two replicas with shared synaptic weights. As in [20], discrete-time dynamics and self-averaging allow us to infer the maximal Lyapunov exponent (MLE) from a single-step expansion rate of the perturbation, but here we need to decompose the perturbation into two components: $\epsilon_i^\alpha(t) = r_i^\alpha(t) + \delta m^\alpha(t)$, with macroscopic perturbation $\delta m^\alpha(t)$ lying in a P -dimensional subspace of the N -dimensional neural activity space and microscopic perturbation $r_i^\alpha(t)$ lying in the $(N - P)$ -dimensional orthogonal complement defined by P constraints $\sum_i r_i^\alpha(t) = 0$. The linearization of (4) around $\epsilon(t) = 0$ gives

$$\epsilon_i^\alpha(t+1) = \phi' \left(\sum_{j,\beta} J_{ij}^{\alpha\beta} x_j^\beta(t) \right) \sum_{j',\beta'} J_{ij'}^{\alpha\beta'} \epsilon_{j'}^{\beta'}(t) \quad (14)$$

where, as before, $J_{ij}^{\alpha\beta} = \frac{\sigma_\mu}{\sqrt{P}} \frac{1}{n} z_i^{\alpha\beta} + \frac{\sigma}{\sqrt{N}} z_{ij}^{\alpha\beta}$. To summarize the evolution of the perturbation within each subspace we define $q^\epsilon(t) = \frac{1}{N} \|\epsilon(t)\|^2$ and $q_m^\epsilon(t) = \frac{1}{N} \|\delta \mathbf{m}(t)\|^2$. In words, $q_m^\epsilon(t)$ and $q^\epsilon(t) - q_m^\epsilon(t)$ denote normalized squared lengths of the perturbation at time t within, respectively, macroscopic and microscopic subspaces. We rewrite (14) as $\epsilon_i^\alpha(t+1) = \eta_i^\alpha(t) \phi'(h_i^\alpha(t))$ where Gaussian fields $h_i^\alpha(t) = \sigma_\mu \sqrt{q_m} \tilde{z}_i^\alpha + \sigma \sqrt{q} \tilde{z}_i^\alpha$ and $\eta_i^\alpha(t) = \sigma_\mu \sqrt{q_m^\epsilon(t)} \tilde{\zeta}_i^\alpha + \sigma \sqrt{q^\epsilon(t)} \tilde{\zeta}_i^\alpha$ are assumed to be independent (i.e., $\tilde{z}_i^\alpha, \tilde{z}_j^\alpha, \tilde{\zeta}_i^\alpha, \tilde{\zeta}_j^\alpha$ are independent standard Gaussian random variables), which follows from the observation that $\mathbf{x}(t)$ and $\epsilon(t)$ are generically expected to be orthogonal. Finally, we average over the Gaussian fields, leading to (see Appendix B for the derivation)

$$\begin{pmatrix} q_m^\epsilon(t+1) \\ q^\epsilon(t+1) - q_m^\epsilon(t+1) \end{pmatrix} = \mathbf{D} \begin{pmatrix} q_m^\epsilon(t) \\ q^\epsilon(t) - q_m^\epsilon(t) \end{pmatrix} \quad (15)$$

with

$$\mathbf{D} = \begin{pmatrix} R_{coherent}^2 & 0 \\ C & R_{random}^2 \end{pmatrix} \quad (16)$$

where $C = (\sigma_\mu^2/\sigma^2 + 1)R_{random}^2 - R_{coherent}^2 \geq 0$ and

$$R_{coherent}^2 = \sigma_\mu^2 \int D\tilde{z} \left[\int D\tilde{z}' (\sigma_\mu \sqrt{q_m} \tilde{z} + \sigma \sqrt{q} \tilde{z}') \right]^2 \quad (17a)$$

$$R_{random}^2 = \sigma^2 \int D\tilde{z} \left[\phi' \left(\sqrt{\sigma_\mu^2 q_m + \sigma^2 q} \tilde{z} \right) \right]^2 \quad (17b)$$

are the eigenvalues of the \mathbf{D} . The long-term evolution of a generic perturbation will be dominated by the larger of the two. Therefore, the MLE can be calculated as $\lambda_{max} = \max(\lambda_{random}, \lambda_{coherent})$ where $\lambda_X = \ln(R_X)$.

The interactions between macroscopic and microscopic dynamics are asymmetric. Although a macroscopic perturbation has a direct effect on microscopic activity, a microscopic perturbation does not transmit to macroscopic activity due to averaging. This translates into the lower-triangular form of \mathbf{D} . Moreover, high-dimensional chaos resulting from chaotic microscopic dynamics can be suppressed by high levels of macroscopic activity. Indeed, the asymptotic behavior of R_{random}^2 for $\sigma_\mu \gg 1$ reads $R_{random}^2 \approx C_0 \sigma^2 / \sqrt{\sigma_\mu^2 q_m + \sigma^2 q}$. Since q_m and q are non-decreasing and bounded functions of σ_μ , for any fixed σ there exists σ_μ^{EoHC} such that for $\sigma_\mu > \sigma_\mu^{EoHC}$ a random perturbation within the $(N - P)$ -dimensional microscopic subspace is contracted ($R_{random}^2 < 1$), i.e. high-dimensional chaos is suppressed. Based on this analysis, we can expect that around σ_μ^{EoHC} the system will transition between low-dimensional and high-dimensional chaos.

Computer simulations.—We test this prediction with computer simulations (see Appendix E for details). In Fig. 1, we present eigenvalues of the weight matrix and example activities of neurons and populations in the four phases predicted by the mean-field theory. In Fig. 3, we illustrate relevant statistics of the dynamics as functions of control parameters.

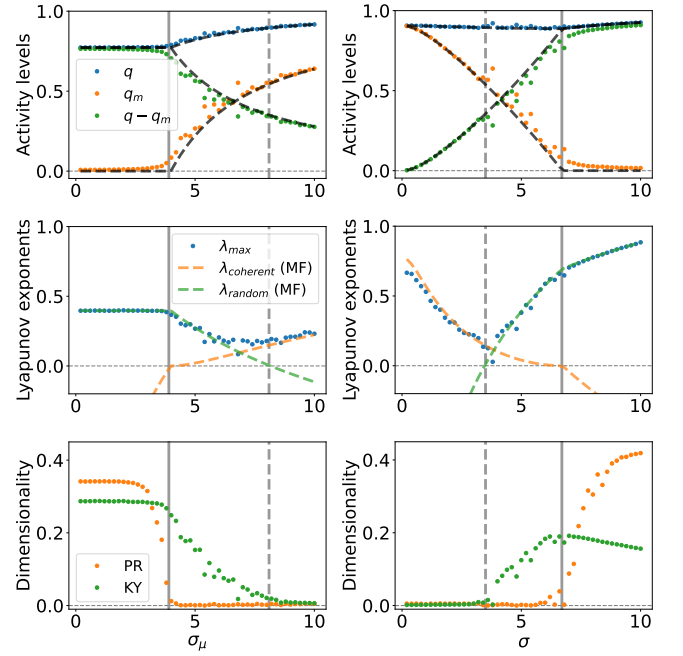


FIG. 3. Statistics of the typical autonomous dynamics as functions of σ_μ for $\sigma = 3.5$ (left) and as functions of σ for $\sigma_\mu = 8$ (right). Dots and dashed lines correspond to results of computer simulations and predictions of the mean-field theory, respectively. Vertical gray lines represent transition lines: $\lambda_{coherent} = 0$ (solid) and $\lambda_{random} = 0$ (dashed). *Top:* Total (q), macroscopic (q_m), and microscopic ($q - q_m$) variances. *Center:* Maximal Lyapunov exponents computed either directly from simulations or as within-subspace theoretical predictions. *Bottom:* Normalized dimensionality of the steady-state neural activity manifold as measured by the covariance matrix (PR dimension) or Lyapunov exponents (KY dimension).

As expected, with fixed $\sigma > 1$ and increasing σ_μ , we observe a region with a substantial drop in the values of the Kaplan-Yorke (KY or Lyapunov) dimension [60–62], where the Lyapunov dimension transitions from being extensive in N to being extensive in P . In contrast, the participation ratio (PR) dimension [52, 63–66] exhibits an abrupt transition around σ_μ^* , leading to a region where these two measures of attractor dimensionality differ by orders of magnitude. A similar region is observed with fixed $\sigma_\mu > 1$ and increasing σ . Additionally, in this case the Lyapunov dimension features a peak and slowly decreases at large values of σ . This effect has been previously noted and explained in the single-population model [67]. Other quantitative predictions of our mean-field analysis are also confirmed by the simulations. In particular, the MLE admits a minimum at intermediate values of σ (for fixed σ_μ) or σ_μ (for fixed σ), suggestive of an effective competition between macroscopic and microscopic dynamics. In other words, both adding modular structure (increasing σ_μ) to mostly random connectivity (large initial σ and small initial σ_μ) and injecting noise (increasing σ) to strongly modular connectivity (large initial σ_μ and small σ) lead to attenuation of chaos. These results are summarized as a phase diagram in Fig. 2. Furthermore, our preliminary simulations confirm that

the same qualitative results are obtained in the continuous-time version of the model [68].

Multilevel generalization.—In biological neural circuits we expect each population to consist of multiple sub-populations, which in turn may be further subdivided into sub-sub-populations, and so on. To capture such a hierarchical connectivity organization we introduce a generalization of our model in the following, recursive manner:

$$\mathbf{J}^{[i]} = \mathbf{J}^{[i-1]} \otimes \mathbf{O}^{(P_i)} + \sigma_i \Xi^{(N_i)} \quad (18)$$

where $N_i = \prod_{j=0}^i P_j$, $P_0 = 1$, $\mathbf{J}^{[0]} = 0$, and σ_i and P_i are parameters specific to level i . Our basic model is equivalent to the case with two levels ($\mathbf{J} = \mathbf{J}^{[2]}$) and $\sigma_1 = \sigma_\mu$, $\sigma_2 = \sigma$, $P_1 = P$, $P_2 = n$.

To facilitate the analysis we make use of tensor notation with indices that specify the unit at each level of the hierarchy. We rewrite the evolution equation as $x_{\alpha_1 \dots \alpha_L}(t+1) = \phi(h_{\alpha_1 \dots \alpha_L}(t))$ with $h_{\alpha_1 \dots \alpha_L}(t) = \sum_{\beta_1 \dots \beta_L} J_{\alpha_1 \dots \alpha_L}^{\beta_1 \dots \beta_L} x_{\beta_1 \dots \beta_L}(t)$, and introduce mean activities at level j as $m_{\alpha_1 \dots \alpha_j}(t) = (N_j/N_L) \sum_{\alpha_{j+1} \dots \alpha_L} x_{\alpha_1 \dots \alpha_L}(t)$. Since we only make use of sums over adjacent right-most indices, this simplified notation does not introduce any ambiguity. We assume $\forall_i P_i \gg 1$ and substitute $\sum_{j=1}^L \sigma_j \sqrt{q_j(t)} z_{\alpha_1 \dots \alpha_j}^{[j]}$ for the preactivations $h_{\alpha_1 \dots \alpha_L}(t)$, where $z_{\alpha_1 \dots \alpha_j}^{[j]}$ are i.i.d. standard normal random variables and $q_j(t) = \frac{1}{N_j} \sum_{\alpha_1 \dots \alpha_j} (m_{\alpha_1 \dots \alpha_j}(t))^2$ are the order parameters that in effect evolve as (see Appendix A for the derivation)

$$q_j(t+1) = \int D\tilde{z} \left(\int Dz \phi \left(\sqrt{A_j(t)} \tilde{z} + \sqrt{A_L(t) - A_j(t)} z \right) \right)^2 \quad (19)$$

where $A_j(t) = \sum_{i=1}^j \sigma_i^2 q_i(t)$. As in the two-level case, here also, each level contributes its own (maximal within the relevant subspace) Lyapunov exponent $\lambda_j = \ln R_i$, which in the mean-field limit can be expressed as (see Appendix B for the derivation)

$$R_j^2 = \sigma_j^2 \int D\tilde{z} \left(\int Dz \phi' \left(\sqrt{A_j} \tilde{z} + \sqrt{A_L - A_j} z \right) \right)^2 \quad (20)$$

where $A_j = \lim_{t \rightarrow \infty} A_j(t)$. In the special case of $\phi(x) = \phi_\infty(x)$ we evaluate all relevant integrals and arrive at closed-form expressions

$$\sigma_j^2 = \frac{2}{\pi q_j} \frac{\sin\left(\frac{\pi}{2} q_j\right) - \sin\left(\frac{\pi}{2} q_{j-1}\right)}{1 - \sin\left(\frac{\pi}{2} q_L\right)} \quad (21)$$

and

$$R_j^2 = \frac{2}{\pi q_j} \frac{\sin\left(\frac{\pi}{2} q_j\right) - \sin\left(\frac{\pi}{2} q_{j-1}\right)}{\cos\left(\frac{\pi}{2} q_j\right)} \quad (22)$$

Eq. (21) specifies a sequence of control parameters that gives rise to a steady state described by an admissible sequence of order parameters $0 = q_0 \leq q_1 \leq q_2 \leq \dots \leq q_L < 1$ [69].

Given the explicit form of (22), we are ready to investigate how the MLE depends on the levels of network activity. Let k be such that $q_{k-1} = 0$ and $q_k > 0$. The corresponding MLE $\lambda_k = \frac{1}{2} \ln \left(\tan\left(\frac{\pi}{2} q_k\right) / \left(\frac{\pi}{2} q_k\right) \right)$ is positive and does not depend on the order parameters at lower levels. Thus, the non-quiescent steady state of this model is always chaotic. However, in deep hierarchical structures with $L \gg 1$ we can expect the overall MLE to be close to zero, as long as many levels are active and approximately balanced, i.e., if $\Delta_j = q_j - q_{j-1}$ are all of the order of q_L/L . For $L \gg 1$ we then have $\Delta_j \ll 1$ and we can expand the level-specific MLEs as $\lambda_k \approx \pi^2 \Delta_k^2 / 24$ and, for $j > k$, $\lambda_j \approx \frac{1}{2} \ln \left(\frac{\Delta_j}{q_j} + \frac{\pi \tan\left(\frac{\pi}{2} q_j\right)}{4 q_j} \Delta_j^2 \right)$ [70]. This demonstrates that $\lambda_{max} \approx 0$ for $L \gg 1$ and $L^2 \gtrsim \tan\left(\frac{\pi}{2} q_L\right)$. Therefore, any mechanism that maintains a loosely balanced hierarchical activity of the network (i.e., with all Δ_j of the order of $1/L$) will also keep it close to the edge of chaos. To illustrate this, we devise and test a proof-of-concept adaption algorithm [71]. Importantly, although our analysis above assumes $\phi(x) = \phi_\infty(x)$, we expect its conclusions to be more general since, due to an effective coarse-graining, the dynamics at higher levels of the hierarchy is universal for a wide range of activation functions (see Appendix D for details).

Conclusion.—We introduced a modular neural network model and studied its autonomous dynamics. We showed that, with increasing correlations between within-population weights, the suppression of high-dimensional chaotic dynamics proceeds in two steps. First, starting from σ_μ^* the macroscopic activity of populations becomes coherent, as signaled by non-zero q_m , positive $\lambda_{coherent}$, and a low value of the participation ratio dimension. At σ_μ^* , critical macroscopic dynamics coexist with non-critical, chaotic microscopic dynamics, analogous to the low-dimensional criticality embedded in high-dimensional neural dynamics recently uncovered in the motor cortex of awake, behaving mice [72]. Second, high-dimensional chaos is completely suppressed above σ_μ^{EoHC} , as signaled by negative λ_{random} and a low value of the Lyapunov dimension. Moreover, the maximal Lyapunov exponent features a prominent dip at intermediate values of weights correlations, indicating that modular synaptic connectivity supports dynamics in the vicinity of the edge of chaos and suggesting an interesting computational regime that maintains the balance between macroscopic and microscopic dynamics. This effect is even more pronounced in the multilevel generalization of the model. We hypothesize that it provides an example of a general mechanism that underpins a potentially ubiquitous phenomenon of complex biological systems evolving towards the edge of chaos through a loose balance of multiscale, hierarchical dynamics. Furthermore, in the brain activities at different levels of hierarchy may encode and process distinct information, with level-specific coherent-quiescent transitions providing a substrate for flexible modulation of information flow.

-
- [1] N. H. Packard, Dynamic patterns in complex systems **212**, 293 (1988).
- [2] C. G. Langton, Physica D: nonlinear phenomena **42**, 12 (1990).
- [3] S. A. Kauffman and S. Johnsen, Journal of theoretical biology **149**, 467 (1991).
- [4] T. Mora and W. Bialek, Journal of Statistical Physics **144**, 268 (2011).
- [5] N. Bertschinger and T. Natschlger, Neural computation **16**, 1413 (2004).
- [6] R. Legenstein and W. Maass, Neural networks **20**, 323 (2007).
- [7] D. Sussillo and L. F. Abbott, Neuron **63**, 544 (2009).
- [8] T. Toyozumi and L. F. Abbott, Physical Review E—Statistical, Nonlinear, and Soft Matter Physics **84**, 051908 (2011).
- [9] S. S. Schoenholz, J. Gilmer, S. Ganguli, and J. Sohl-Dickstein, arXiv preprint arXiv:1611.01232 (2016).
- [10] J. Schuecker, S. Goedeke, and M. Helias, Physical Review X **8**, 041029 (2018).
- [11] A. V. Herz and J. J. Hopfield, Physical review letters **75**, 1222 (1995).
- [12] D. Stassinopoulos and P. Bak, Physical Review E **51**, 5033 (1995).
- [13] D. R. Chialvo and P. Bak, Neuroscience **90**, 1137 (1999).
- [14] O. Kinouchi and M. Copelli, Nature physics **2**, 348 (2006).
- [15] J. M. Beggs, Philosophical Transactions of the Royal Society A: Mathematical, Physical and Engineering Sciences **366**, 329 (2008).
- [16] J. M. Beggs and N. Timme, Frontiers in physiology **3**, 163 (2012).
- [17] M. A. Munoz, Reviews of Modern Physics **90**, 031001 (2018).
- [18] A. J. Fontenele, N. A. De Vasconcelos, T. Feliciano, L. A. Aguiar, C. Soares-Cunha, B. Coimbra, L. Dalla Porta, S. Ribeiro, A. J. Rodrigues, N. Sousa, *et al.*, Physical review letters **122**, 208101 (2019).
- [19] D. M. Castro, T. Feliciano, N. A. P. de Vasconcelos, C. Soares-Cunha, B. Coimbra, A. J. a. Rodrigues, P. V. Carelli, and M. Copelli, PRX Life **2**, 023008 (2024).
- [20] L. Molgedey, J. Schuchhardt, and H. G. Schuster, Physical review letters **69**, 3717 (1992).
- [21] K. Rajan, L. Abbott, and H. Sompolinsky, Physical Review E—Statistical, Nonlinear, and Soft Matter Physics **82**, 011903 (2010).
- [22] S. Takasu and T. Aoyagi, Physical Review Research **6**, 013172 (2024).
- [23] K. Rajan and L. F. Abbott, Physical review letters **97**, 188104 (2006).
- [24] T. Cabana and J. Touboul, Journal of Statistical Physics **153**, 211 (2013).
- [25] J. Aljadeff, M. Stern, and T. Sharpee, Physical review letters **114**, 088101 (2015).
- [26] I. D. Landau and H. Sompolinsky, PLoS computational biology **14**, e1006309 (2018).
- [27] F. Mastroiuseppe and S. Ostojic, Neuron **99**, 609 (2018).
- [28] U. Pereira-Obilinovic, J. Aljadeff, and N. Brunel, Physical Review X **13**, 011009 (2023).
- [29] D. Mastrovito, Y. H. Liu, L. Kusmierz, E. Shea-Brown, C. Koch, and S. Mihalas, bioRxiv (2024).
- [30] D. G. Clark and M. Beiran, arXiv preprint arXiv:2402.12188 (2024).
- [31] L. De Arcangelis, C. Perrone-Capano, and H. J. Herrmann, Physical review letters **96**, 028107 (2006).
- [32] A. Levina, J. M. Herrmann, and T. Geisel, Nature physics **3**, 857 (2007).
- [33] W. L. Shew, W. P. Clawson, J. Pobst, Y. Karimipannah, N. C. Wright, and R. Wessel, Nature Physics **11**, 659 (2015).
- [34] R. Zeraati, V. Priesemann, and A. Levina, Frontiers in Physics **9**, 619661 (2021).
- [35] D. Dahmen, S. Grun, M. Diesmann, and M. Helias, Proceedings of the National Academy of Sciences **116**, 13051 (2019).
- [36] C. Zhou, L. Zemanova, G. Zamora, C. C. Hilgetag, and J. Kurths, Physical review letters **97**, 238103 (2006).
- [37] Y. He, J. Wang, L. Wang, Z. J. Chen, C. Yan, H. Yang, H. Tang, C. Zhu, Q. Gong, Y. Zang, *et al.*, PloS one **4**, e5226 (2009).
- [38] D. Meunier, R. Lambiotte, A. Fornito, K. Ersche, and E. T. Bullmore, Frontiers in neuroinformatics **3**, 571 (2009).
- [39] D. Meunier, R. Lambiotte, and E. T. Bullmore, Frontiers in neuroscience **4**, 200 (2010).
- [40] O. Sporns and R. F. Betzel, Annual review of psychology **67**, 613 (2016).
- [41] J. A. Harris, S. Mihalas, K. E. Hirokawa, J. D. Whitesell, H. Choi, A. Bernard, P. Bohn, S. Caldejon, L. Casal, A. Cho, *et al.*, Nature **575**, 195 (2019).
- [42] B. Tasic, Z. Yao, L. T. Graybuck, K. A. Smith, T. N. Nguyen, D. Bertagnolli, J. Goldy, E. Garren, M. N. Economo, S. Viswanathan, *et al.*, Nature **563**, 72 (2018).
- [43] H. Zeng, Cell **185**, 2739 (2022).
- [44] D. J. Felleman and D. C. Van Essen, Cerebral cortex (New York, NY: 1991) **1**, 1 (1991).
- [45] Y. LeCun, Y. Bengio, and G. Hinton, nature **521**, 436 (2015).
- [46] I. Goodfellow, Y. Bengio, and A. Courville, *Deep Learning* (MIT Press, 2016) <http://www.deeplearningbook.org>.
- [47] M. Pascual and J. A. Dunne, *Ecological networks: linking structure to dynamics in food webs* (Oxford University Press, 2006).
- [48] M. Rubinov, O. Sporns, J.-P. Thivierge, and M. Breakspear, PLoS computational biology **7**, e1002038 (2011).
- [49] S.-J. Wang and C. Zhou, New Journal of Physics **14**, 023005 (2012).
- [50] P. Moretti and M. A. Munoz, Nature communications **4**, 2521 (2013).
- [51] H. Sompolinsky, A. Crisanti, and H.-J. Sommers, Physical review letters **61**, 259 (1988).
- [52] D. G. Clark, L. Abbott, and A. Litwin-Kumar, Physical Review Letters **131**, 118401 (2023).
- [53] B. Poole, S. Lahiri, M. Raghu, J. Sohl-Dickstein, and S. Ganguli, Advances in neural information processing systems **29** (2016).
- [54] S. Allesina, J. Grilli, G. Barabas, S. Tang, J. Aljadeff, and A. Maritan, Nature communications **6**, 7842 (2015).
- [55] F. Roy, G. Biroli, G. Bunin, and C. Cammarota, Journal of Physics A: Mathematical and Theoretical **52**, 484001 (2019).
- [56] G. Garcia Lorenzana, A. Altieri, and G. Biroli, PRX Life **2**, 013014 (2024).
- [57] P. Arbenz and G. H. Golub, SIAM Journal on Matrix Analysis and Applications **9**, 40 (1988).
- [58] T. Tao, Probability Theory and Related Fields **155**, 231 (2013).
- [59] This assumption could be easily relaxed. In general, each block could be rectangular, reflecting different sizes of populations. The results would not be affected as long as the number of neurons in each population is large enough to justify the validity of the mean-field approach utilized in our analysis.
- [60] J. L. Kaplan and J. A. Yorke, in *Functional Differential Equations and Approximation of Fixed Points: Proceedings, Bonn, July 1978* (Springer, 1979) pp. 204–227.
- [61] P. Frederickson, J. L. Kaplan, E. D. Yorke, and J. A. Yorke, Journal of differential equations **49**, 185 (1983).

- [62] E. Ott, *Chaos in dynamical systems* (Cambridge university press, 2002).
- [63] K. Rajan, L. Abbott, and H. Sompolinsky, *Advances in Neural Information Processing Systems* **23** (2010).
- [64] P. Gao, E. Trautmann, B. Yu, G. Santhanam, S. Ryu, K. Shenoy, and S. Ganguli, *BioRxiv*, 214262 (2017).
- [65] S. Recanatesi, G. K. Ocker, M. A. Buice, and E. Shea-Brown, *PLoS computational biology* **15**, e1006446 (2019).
- [66] S. Recanatesi, S. Bradde, V. Balasubramanian, N. A. Steinmetz, and E. Shea-Brown, *Patterns* **3** (2022).
- [67] R. Engelken, F. Wolf, and L. F. Abbott, *Physical Review Research* **5**, 043044 (2023).
- [68] To be published elsewhere.
- [69] This sequence is not unique when some of the highest-level activities are set to zero, i.e. $q_1 = q_2 = \dots = q_j = 0$. In this case, the corresponding limiting values of $\sigma_1 = \sigma_2 = \dots = \sigma_j$ specify the maximum values of these parameters (phase boundary),

as any subsequence $(\sigma_i)_{i=1}^j$ within the j -dimensional hypercube leads to the same values of $(q_i)_{i=1}^L$.

- [70] In the latter case we retain two terms since the quadratic term may dominate for large q_j and finite L .
- [71] See Supplementary Material for details.
- [72] A. J. Fontenele, J. S. Sooter, V. K. Norman, S. H. Gautam, and W. L. Shew, *Science Advances* **10**, eadj9303 (2024).
- [73] R. Vogt, M. Puelma Touzel, E. Shlizerman, and G. Lajoie, *Frontiers in Applied Mathematics and Statistics* **8**, 818799 (2022).
- [74] G. Van Rossum and F. L. Drake, *Python 3 Reference Manual* (CreateSpace, Scotts Valley, CA, 2009).
- [75] J. Bradbury, R. Frostig, P. Hawkins, M. J. Johnson, C. Leary, D. Maclaurin, G. Necula, A. Paszke, J. VanderPlas, S. Wanderman-Milne, and Q. Zhang, *JAX: composable transformations of Python+NumPy programs* (2018).

END MATTER

Appendix A: Derivation of (19)

As noted in the main text, we rewrite the evolution equation as

$$x_{\alpha_1 \dots \alpha_L}(t+1) = \phi \left(\sum_{j=1}^L \sigma_j \sqrt{q_j(t)} z_{\alpha_1 \dots \alpha_j}^{[j]} \right) \quad (23)$$

where $z_{\alpha_1 \alpha_2 \dots \alpha_j}^{[j]} \sim \mathcal{N}(0, 1)$ are i.i.d. This decomposition originates from the hierarchical structure of the weight matrix, which contains a sum over L levels, each contributing an independent source of variability:

$$J_{\alpha_1 \dots \alpha_L}^{\beta_1 \dots \beta_L} = \sum_{j=1}^L \frac{1}{P_{j+1} \dots P_L} \frac{\sigma_j}{\sqrt{N_j}} z_{\alpha_1 \dots \alpha_j \beta_1 \dots \beta_j}^{[j]} \quad (24)$$

where $z_{\alpha_1 \dots \alpha_j \beta_1 \dots \beta_j}^{[j]} \sim \mathcal{N}(0, 1)$ are all independent. Equation (23) follows immediately from

$$\sum_{\beta_1 \dots \beta_L} \frac{1}{P_{j+1} \dots P_L} \frac{1}{\sqrt{N_j}} z_{\alpha_1 \dots \alpha_j \beta_1 \dots \beta_j}^{[j]} x_{\beta_1 \dots \beta_L}(t) = \sqrt{q_j(t)} z_{\alpha_1 \dots \alpha_j}^{[j]} \quad (25)$$

Our goal is to find an evolution equation of

$$q_j(t) = \frac{1}{P_1 \dots P_j} \sum_{\alpha_1, \dots, \alpha_j} (m_{\alpha_1 \dots \alpha_j}(t))^2 \quad (26)$$

where

$$m_{\alpha_1 \dots \alpha_j}(t) = \frac{1}{P_{j+1} \dots P_L} \sum_{\alpha_{j+1}, \dots, \alpha_L} x_{\alpha_1 \dots \alpha_L}(t) \quad (27)$$

We start by rewriting (27) at time $t+1$ using (23)

$$m_{\alpha_1 \dots \alpha_j}(t+1) = \frac{1}{P_{j+1} \dots P_L} \sum_{\alpha_{j+1}, \dots, \alpha_L} \phi \left(\sum_{i=1}^L \sigma_i \sqrt{q_i(t)} z_{\alpha_1 \dots \alpha_i}^{[i]} \right) \quad (28)$$

We note that all terms under the activation function with $i > j$ contain at least a single index α_k that is averaged over, which in the limit of $P_k \rightarrow \infty$ converges to the expectation over the corresponding standard normal variable. In contrast, terms with $i \leq j$ do not contain summation indices $\alpha_{j+1}, \dots, \alpha_L$ and are not affected by the averaging. Thus, the right-hand side (RHS) of (28) can be rewritten as

$$\int_{\mathbb{R}^{L-j}} Dz_{j+1} \dots Dz_L \phi \left(\sum_{i=1}^j \sigma_i \sqrt{q_i(t)} z_{\alpha_1 \dots \alpha_i}^{[i]} + \sum_{k=j+1}^L \sigma_k \sqrt{q_k(t)} z_k \right) \quad (29)$$

where $Dz_i = dz_i \exp(-z_i^2/2) / \sqrt{2\pi}$. Due to the stability of the Gaussian distribution (convolutions of Gaussian distributions are still Gaussian), we can replace the expectation of a function of a sum of Gaussian random variables with an expectation of the same function over a properly scaled single Gaussian random variable, i.e.

$$\int_{\mathbb{R}^n} Dz_1 \dots Dz_n f \left(\sum_{i=1}^n a_i z_i \right) = \int_{\mathbb{R}} Dz f \left(z \sqrt{\sum_{i=1}^n a_i^2} \right), \quad (30)$$

reducing (28) to

$$m_{\alpha_1 \dots \alpha_j}(t+1) = \int_{\mathbb{R}} Dz \phi \left(\sum_{i=1}^j \sigma_i \sqrt{q_i(t)} z_{\alpha_1 \dots \alpha_i}^{[i]} + \sqrt{A_L(t) - A_j(t)} z \right) \quad (31)$$

where $A_k(t) = \sum_{i=1}^k \sigma_i^2 q_i(t)$. In the final step we plug (31) into (26), repeat the process of replacing averages with expected values, and subsequently replacing expectations over multiple Gaussian random variables with an expected value over a single Gaussian random variable.

Appendix B: Derivation of (20)

Similarly to the basic two-level model, we introduce an infinitesimal perturbation $\epsilon_{\alpha_1 \dots \alpha_L}(t)$ and linearize the evolution

equation (4), arriving at a linear evolution equation for the perturbation

$$\epsilon_{\alpha_1 \dots \alpha_L}(t+1) = \phi' \left(\sum_{\beta_1 \dots \beta_L} J_{\alpha_1 \dots \alpha_L \beta_1 \dots \beta_L}^{\beta_1 \dots \beta_L} x_{\beta_1 \dots \beta_L}(t) \right) \sum_{\gamma_1 \dots \gamma_L} J_{\alpha_1 \dots \alpha_L \gamma_1 \dots \gamma_L}^{\gamma_1 \dots \gamma_L} \epsilon_{\gamma_1 \dots \gamma_L}(t) \quad (32)$$

In analogy to the order parameters used to describe network activity, we introduce

$$m_{\alpha_1 \dots \alpha_j}^\epsilon(t) = \frac{1}{P_{j+1} \dots P_L} \sum_{\alpha_{j+1} \dots \alpha_L} \epsilon_{\alpha_1 \dots \alpha_L}(t) \quad (33)$$

and

$$q_j^\epsilon(t) = \frac{1}{P_1 \dots P_j} \sum_{\alpha_1 \dots \alpha_j} (m_{\alpha_1 \dots \alpha_j}^\epsilon(t))^2. \quad (34)$$

We replace both sums in (32) with Gaussian fields

$$\epsilon_{\alpha_1 \dots \alpha_L}(t+1) = \phi' \left(\sum_{j=1}^L \sigma_j \sqrt{q_j(t)} z_{\alpha_1 \dots \alpha_j}^{[j]} \right) \sum_{k=1}^L \sigma_k \sqrt{q_k(t)} z_{\alpha_1 \dots \alpha_k}^{[k]}. \quad (35)$$

Crucially, we assume that $z_{\alpha_1 \dots \alpha_j}^{[j]}$ and $z_{\alpha_1 \dots \alpha_j}^{[k]}$ are independent, which follows from the assumption that $\mathbf{x}(t)$ and $\epsilon(t)$ are generically orthogonal within any of the considered subspaces (at each level of coarse-graining). Given this assumption, we can replace averages with expectations over independent Gaussian random variables. After straightforward manipulations we arrive at

$$q_j^\epsilon(t+1) = A_j^\epsilon(t) \int_{-\infty}^{\infty} D\tilde{z} \left(\int_{-\infty}^{\infty} Dz \phi' \left(\sqrt{A_j(t)} \tilde{z} + \sqrt{A_L(t) - A_j(t)} z \right) \right)^2 \quad (36)$$

where $A_j^\epsilon(t) = \sum_{i=1}^j \sigma_i^2 q_i^\epsilon(t)$ comes from the term $\sum_{k=1}^L \sigma_k \sqrt{q_k^\epsilon(t)} z_{\alpha_1 \dots \alpha_k}^{[k]}$. In the steady-state, $q_j = \lim_{t \rightarrow \infty} q_j(t)$ and $A_j = \lim_{t \rightarrow \infty} A_j(t)$ are constant and (36) is linear dynamical system of the form $\mathbf{q}^\epsilon(t+1) = \mathbf{D} \mathbf{q}^\epsilon(t)$, where \mathbf{D} is an $L \times L$ time-independent triangular matrix. Its diagonal entries correspond exactly to its eigenvalues and are given by (20).

Appendix C: Relevant integrals

In order to derive (21) and (22) from (19) and (20) we used the following identities:

$$\int_{\mathbb{R}} Dz \phi_\infty(az+b) = \phi_\infty \left(\frac{b}{\sqrt{1+\pi a^2/2}} \right) \quad (37)$$

$$\int_{\mathbb{R}} Dz (\phi_\infty(cz))^2 = \frac{4}{\pi} \arctan(\sqrt{1+\pi c^2}) - 1 \quad (38)$$

To prove (37), we introduce $f(a,b) = \int_{\mathbb{R}} Dz \phi_\infty(az+b)$ and calculate $\partial_b f(a,b)$. Since $\phi'_\infty(x) = \exp(-\pi x^2/4)$, this results in a

Gaussian integral (over the entire real line) which is straightforward to evaluate, leading to

$$\partial_b f(a,b) = \frac{1}{\sqrt{1+\frac{\pi}{2}a^2}} \exp \left(-\frac{\frac{\pi}{4}b^2}{1+\frac{\pi}{2}a^2} \right) \quad (39)$$

Thus, $f(a,b)$ is given by the indefinite Gaussian integral

$$f(a,b) = \phi_\infty \left(\frac{b}{\sqrt{1+\pi a^2/2}} \right) + C(a) \quad (40)$$

where $C(a)$ is an unknown function of a . Finally, due to the fact that ϕ_∞ is odd we find that $C(a) = f(a,0) = 0$. ■

To prove (38), we introduce $g(c) = \int Dz [\phi_\infty(cz)]^2$ and calculate its derivative

$$g'(c) = \sqrt{\frac{2}{\pi}} \int_{-\infty}^{\infty} dz \exp \left(-\frac{z^2}{2} \left(1 + \frac{\pi}{2} c^2 \right) \right) z \phi_\infty(cz) \quad (41)$$

We rewrite the RHS of (41) as

$$\sqrt{\frac{2}{\pi}} \int_{-\infty}^{\infty} dz \frac{d}{dz} \left[-\frac{1}{1+\frac{\pi}{2}c^2} \exp \left(-\frac{z^2}{2} \left(1 + \frac{\pi}{2} c^2 \right) \right) \right] \phi_\infty(cz) \quad (42)$$

and, applying integration by parts, arrive at

$$g'(c) = \frac{2c}{\left(1 + \frac{\pi}{2} c^2 \right) \sqrt{1+\pi c^2}} \quad (43)$$

Next, we set $u = \sqrt{1+\pi c^2}$ and perform integration by substitution, which gives

$$g(c) = \frac{4}{\pi} \arctan(\sqrt{1+\pi c^2}) + C_0 \quad (44)$$

To find the value of C_0 , we observe that $g(0) = 0$ (since $\phi_\infty(0) = 0$), from which we infer $C_0 = -1$. ■

Appendix D: Universality

Assume ϕ to be odd with $\phi(\infty) = 1$ and a single-peaked ϕ' . If most lower levels contribute to the activity of the multilevel system, we have $\sigma_i > 1$ for most levels. Thus, at high-enough levels of the hierarchy, $j \ll L$, we have $A_L - A_j \gg 1$ and the limit $\lim_{a \rightarrow \infty} a \phi'(ax) = 2\delta(x)$ provides a way of approximating (19) and (20) as

$$q_j(t+1) \approx \int Dz (\phi_\infty(B_j(t)z))^2 \quad (45)$$

and

$$R_j^2 \approx \tilde{\sigma}_j^2 \int Dz (\phi'_\infty(B_j z))^2, \quad (46)$$

where $\tilde{\sigma}_j^2 = \frac{2}{\pi} \frac{\sigma_j^2}{A_L - A_j}$, $B_j(t) = \sqrt{\frac{2}{\pi}} \sqrt{\frac{A_j(t)}{A_L(t) - A_j(t)}}$, $B_j = \lim_{t \rightarrow \infty} B_j(t)$, and $\phi_\infty(x) = \lim_{a \rightarrow \infty} \phi_a(x)$ is given

by (11). Due to (37), the two formulas above match the mean-field equations for a multilevel system with the activation function set to ϕ_∞ . Indeed, direct computations similar to (10) confirm that ϕ_∞ is the activation function of the effective evolution of the higher level activities. In other words, ϕ_∞ is a fixed point of the coarse-graining procedure for a wide range of underlying microscopic activation functions. This illustrates the special status of ϕ_∞ as the effective activation function of higher, population level activities, and it provides a justification for the expectation that our results extend with no qualitative changes to many activation functions.

Appendix E: Details of the computer simulations

Fig. 1: For visualization purposes, network sizes differed between weight visualizations ($n = 8, P = 8$), eigenvalues panels ($n = 5, P = 200$), and the simulations ($n = 200, P = 100$). Networks were simulated for 220 steps starting from random initial conditions, with activities from the last 20 steps used for plotting. The random seed was shared across columns. In Fig. 3, recurrent neural networks with $P = n = 100$ were simulated for 22000 steps starting from random initial conditions (i.i.d. $x_i^\alpha \sim \mathcal{N}(0, 1)$). Weights and initial conditions were reinitialized for each pair of values of control parameters (σ, σ_μ) . In order to ensure that the statistics were collected close to the steady state, first 2000 steps were discarded. Network activity at all remaining 20000 steps were used to calculate q , q_m , and the participation ratio dimension. Network activity during the last 500 steps were used to compute Lyapunov exponents and the associated Lyapunov dimension. Dimensionalities were normalized by the total number of neurons (10^4). For numerical stability, QR decomposition was used in computations of the Lyapunov exponents; for details of the algorithm see [73]. The code, available online at <https://github.com/AllenInstitute/modular-networks-theory>, was written in Python [74] utilizing JAX [75] for GPU acceleration.

Supplementary Material: Hierarchy of chaotic dynamics in random modular networks

Łukasz Kuśmierz,¹ Ulises Pereira-Obilinovic,¹ Zhixin Lu,¹ Dana Mastrovito,¹ and Stefan Mihalas¹

¹Allen Institute, Seattle, WA

$\sigma(\Delta)$ ADAPTATION ALGORITHM

In the main text, we argue that an adaptation algorithm driving the system toward a balance across hierarchical activity levels naturally positions it near the edge of chaos. To support this claim, here we introduce and test a simple adaptation algorithm. It is important to note that the algorithm presented here serves as a proof of concept rather than a specific model that we propose the brain, or any natural system, implements.

The algorithm is based on the observation that a hierarchical modular system with L levels should be close to the edge of chaos as long as $\Delta_i = q_i - q_{i-1}$ are all of the order of q_L/L , where q_L is the total activity variance of the network. Thus, given a desired total level of activity \hat{q}_L , we set the desired within-level activities to

$$\hat{\Delta}_i = \frac{\hat{q}_L}{L} \quad (47)$$

We assume that the synaptic weights are drawn randomly according to the multilevel version of our connectivity model (18), but with a time-dependent level-specific control parameters $\sigma_i(t)$, i.e.

$$\mathbf{J}^{[i]}(t) = \mathbf{J}^{[i-1]}(t) \otimes \mathbf{O}^{(P_i)} + \sigma_i(t) \mathbf{\Xi}^{(N_i)} \quad (48)$$

For simplicity, the individual entries $\mathbf{\Xi}^{(N_i)}$ are fixed. At each time step of the adaptation process, $\Delta_i(t)$ are computed based on the network activity $\mathbf{x}(t)$, and $\sigma_i(t)$ are updated according to

$$\sigma_i(t+1) = \sigma_i(t) + \eta (\hat{\Delta}_i - \Delta_i(t)) \quad (49)$$

where η is a fixed learning rate. Equation (49) was not derived from any cost function. Instead, it is based on the intuitive observation that, all else being equal, Δ_i is expected to be a non-decreasing function of σ_i . Note also that our choice of $\hat{\Delta}_i$ is somewhat arbitrary and is not actually optimal, i.e. it does not minimize the maximal Lyapunov exponent for a given \hat{q}_L . Nonetheless, as we argue in the main text, it should still lead to low (and positive) values of the maximal Lyapunov exponent if L is large enough. Our numerical experiments, described in detail below, show that this is already true even for $L = 2$ and $L = 3$, as long as q_L is not too close to 1.

First, we test whether our adaptation algorithm brings the activity levels q_i close to the desired values $\hat{q}_k = kq_L/L$. In two-level networks the order parameters quickly converge to the steady state, where they fluctuate around the set point (Fig. 4, top). The associated values of the control parameters feature lower level of fluctuations whose means are close to, but may not match exactly, the values predicted by the mean-field theory (Fig. 4, bottom). The fluctuations and the bias are expected to be finite-size effects. The results are similar in three-level networks (Fig. 5). Occasionally, all order and control parameters seem to converge to values slightly larger than desired. This happens because in these networks q_0 , which denotes the squared mean activity of the network, converges to a significant non-zero values. Our algorithm does not attempt control q_0 , since in our simple formulation of the model there is no associated control parameter and in the thermodynamic limit q_0 is predicted to be equal to 0 anyway. Given that Δ_1 is calculated as $q_1 - q_0$, the convergence of all Δ_i to \hat{q}_L/L does not imply the convergence of all q_i to $i\hat{q}_L/L$. Instead, q_i converges to $i\hat{q}_L/L + q_0$. This phenomenon can lead to a failure of the algorithm when $\hat{q}_L + q_0 > 1$, which we occasionally observe in four-level networks when the number of populations is relatively small (Fig. 6). However, we expect this to be a finite-size effect that does not persist in larger networks. Indeed, increasing the number of populations in four-level networks seems to significantly reduce the effect (Fig. 7).

We repeat this procedure for various values of \hat{q}_L , as summarized in Fig. 8. As expected, the adaptation process drives q_L close to \hat{q}_L and, in most cases, brings σ_L to values predicted by the mean-field theory. The only exception is for $L = 4$, where the σ_L resulting from the adaptation remains significantly larger than the mean-field prediction, presumably due to finite-size effects. Given that our algorithm successfully balances activity across levels, we expect it to position the system near the edge of chaos. The right panel of Fig. 8 confirms this, showing that the maximal Lyapunov exponents remain significantly closer to 0 for modular networks ($L = 2$ and $L = 3$) compared to homogeneous networks ($L = 1$). The estimated values of λ_{max} align with the mean-field predictions, although modular networks exhibit relatively large variability across realizations. Despite these finite-size effects, we conclude that balancing activity across levels in modular networks places neural dynamics in the vicinity of the edge of chaos.

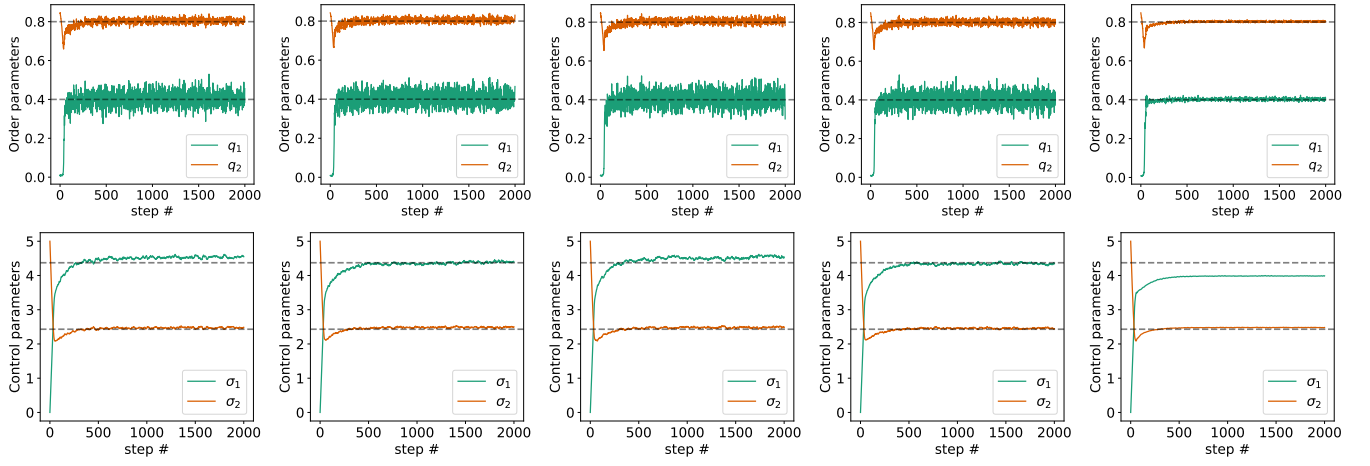


FIG. 4. Evolution of order (*top*) and control (*bottom*) parameters during the adaptation process in networks with two levels ($P_1 = P_2 = 100$). Five columns correspond to different seeds (i.e., independent realizations of the weights and initial conditions). Dashed lines denote the desired activity levels (*top*) and the corresponding control parameters, as predicted by the mean-field equations (*bottom*). Other parameters: $\eta = 0.2$, $\hat{q}_L = 0.8$.

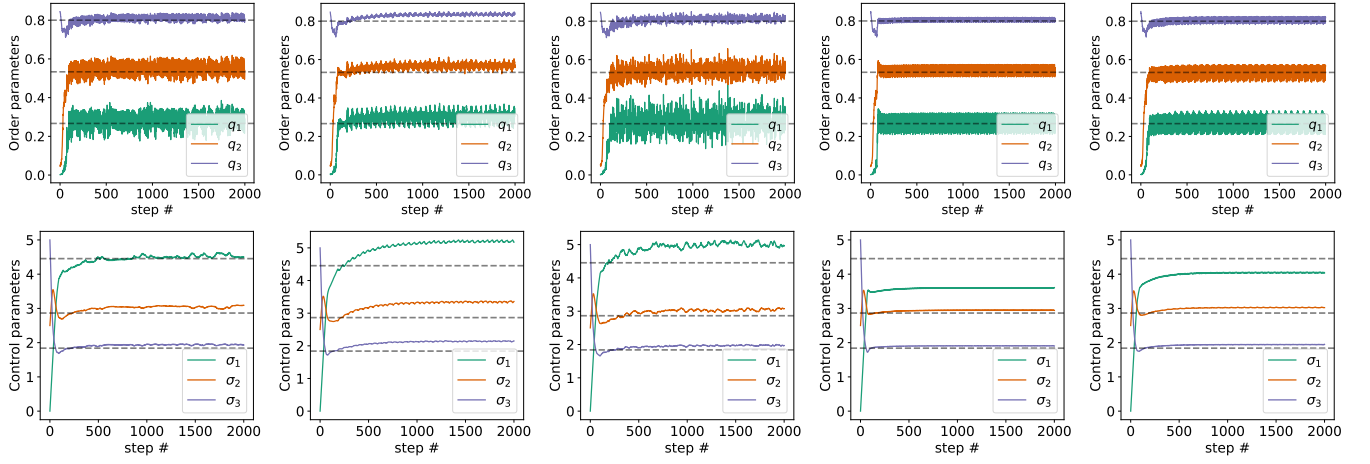


FIG. 5. Same as Fig. 4 but in networks with three levels ($P_1 = P_2 = P_3 = 22$).

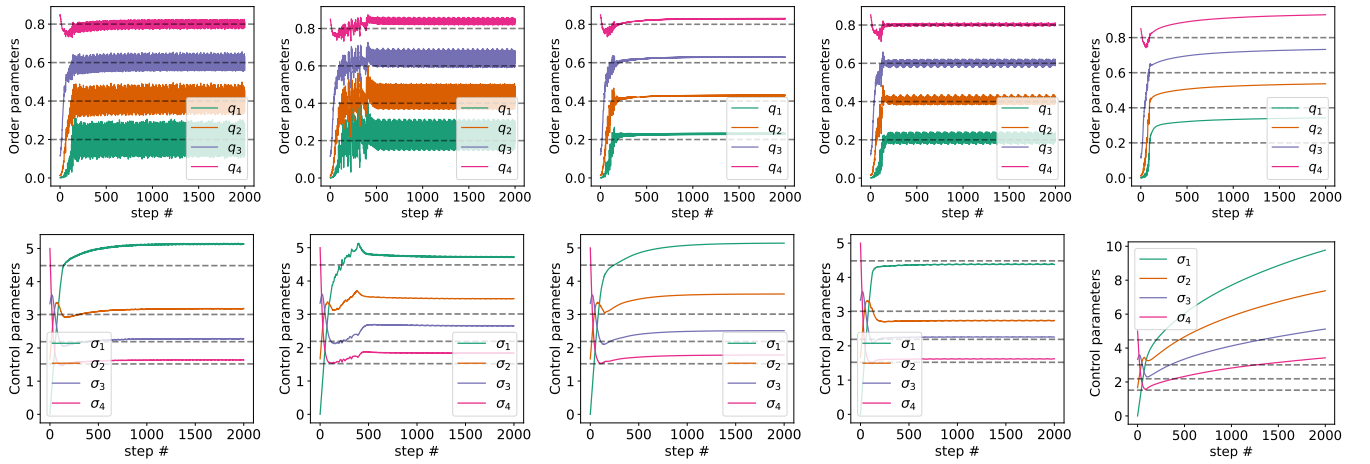


FIG. 6. Same as Fig. 4 but in networks with four levels ($P_1 = P_2 = P_3 = P_4 = 10$).

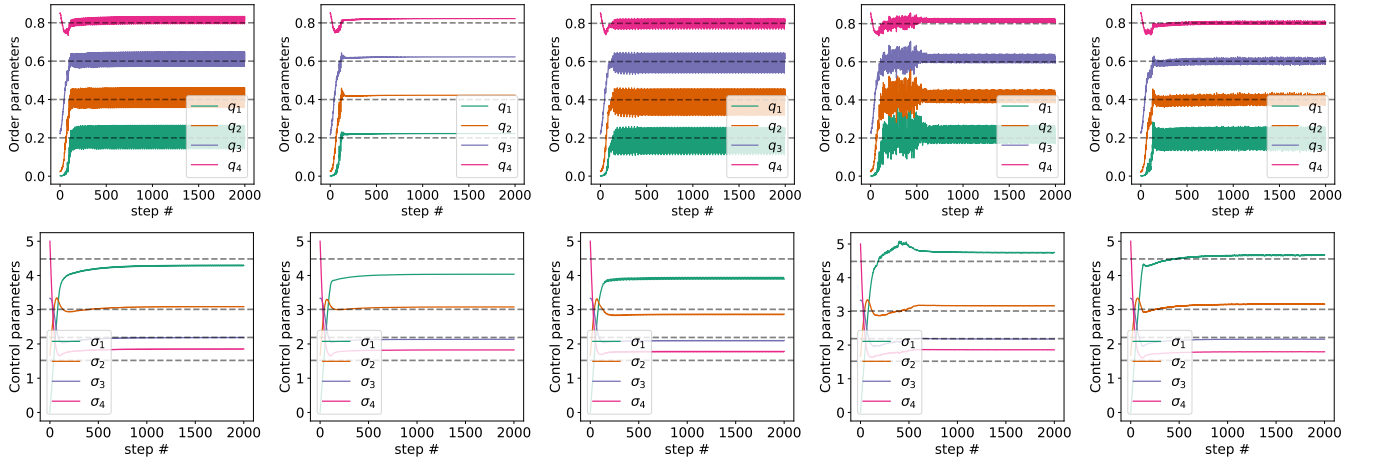


FIG. 7. Same as Fig. 6 but in larger networks with significantly more top-level populations ($P_1 = 20$, $P_2 = 15$, $P_3 = 10$, $P_4 = 5$).

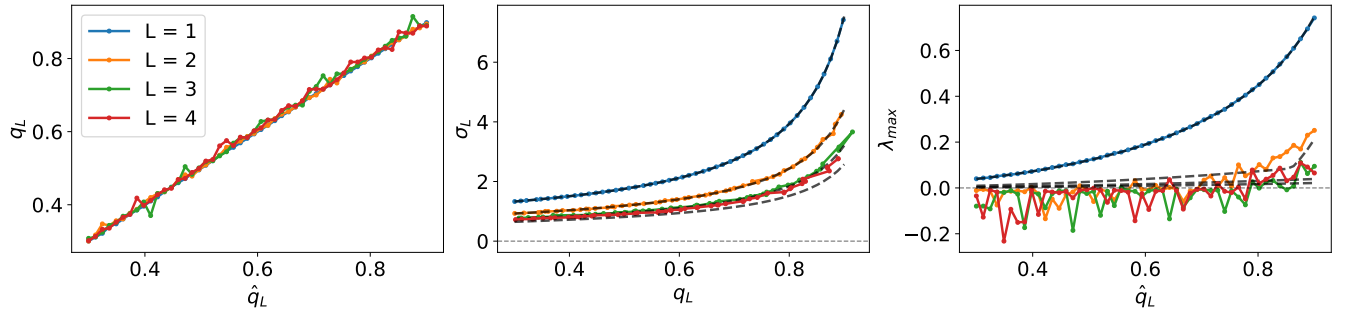


FIG. 8. Values of q_L (left), σ_L (center), and the maximal Lyapunov exponent (right) at the end of the adaptation process as functions of \hat{q}_L or q_L for $L = 1$ ($P_1 = 10^4$), $L = 2$ ($P_1 = P_2 = 100$), $L = 3$ ($P_1 = P_2 = P_3 = 22$), and $L = 4$ ($P_1 = 20$, $P_2 = P_3 = 10$, $P_4 = 5$). The adaptation process runs for 1000 steps, after which control parameters are frozen and the simulation is restarted from a new random initial condition for 700 steps. The last 350 steps are used for estimating the order parameters q_i , whereas the last 200 steps are used for estimating λ_{max} .